DURABILITY OF GFRP-CONCRETE ADHESIVELY BONDED CONNECTIONS: EXPERIMENTAL AND NUMERICAL STUDIES

José A. Gonilha[a*], João R. Correia[a], Fernando A. Branco[a], José Sena-Cruz[b]

[a] CERIS, Instituto Superior Técnico, Universidade de Lisboa, Av. Rovisco Pais 1, 1049-001 Lisboa, Portugal.

[b] ISISE, School of Engineering, University of Minho, Campus de Azurém, 4800-058 Guimarães, Portugal.

[*] corresponding author: e-mail: jose.gonilha@tecnico.ulisboa.pt

tel.: (+351) 218 418 430; fax: (+351) 218 499 242.

Abstract: In order to overcome the main mechanical drawbacks of GFRP profiles, namely their high deformability and proneness to instability phenomena, several GFRP-concrete hybrid solutions comprising bonded connections with epoxy adhesive have been proposed. Although being able to provide almost full interaction at the GFRP-concrete interface(s) (at least in the short-term), there is very little information about the durability of such connection systems, which raises concerns about the long-term performance of hybrid structural solutions. This paper presents experimental and numerical investigations on the durability of adhesively bonded connections between pultruded GFRP profiles and steel fibre reinforced self-compacting concrete (SFRSCC). GFRP-SFRSCC specimens were first subjected to accelerated ageing, involving thermal and wet-dry cycles, and then subjected to push-out tests. The accelerated ageing did not have significant influence on the strength of the GFRP-SFRSCC connection; however, it had a very deleterious effect

on its stiffness. The numerical study included the development of finite element models of the specimens tested. Using bi-linear bond-slip laws, it was possible to simulate the test results with good accuracy. In the final part of the paper, the influence of the interface stiffness reduction on the deformability of a real hybrid structure (the São Silvestre footbridge) is analysed. Although the stiffness of the GFRP-SFRSCC interface is considerably reduced by the ageing processes, this results in a very small increase of the overall mid-span deflections of the footbridge.

Keywords: GFRP, SFRSCC, hybrid structures, epoxy, bonded connections, ageing, push-out tests, FE models, bond-slip laws.

1. INTRODUCTION

Fibre reinforced polymer (FRP) materials are being increasingly considered as an alternative to traditional materials for civil engineering structural applications, due to their high strength, low self-weight, ease of installation, electromagnetic transparency and good chemical and corrosion resistance [1-3]. With low maintenance requirements, these materials offer a promising alternative for the development of more durable and sustainable structures [4].

Pultruded glass-fibre reinforced polymer (GFRP) profiles combine the above mentioned advantages with moderately low manufacturing costs. However, GFRP profiles present low elasticity and shear moduli, being relatively deformable and prone to instability phenomena.

To overcome those limitations, several hybrid structural solutions have been proposed (*e.g.* [5-12]), combining GFRP profiles with concrete elements. In some hybrid solutions,

adhesively bonded (epoxy) connections are used to enhance the composite action, thus preventing the occurrence of interconnection slip at the GFRP-concrete interface(s) [10]. In some cases, adhesive bonding is complemented with mechanical connection systems, which generally provide a negligible contribution to the stiffness (*e.g.* [5-9]), but can act as a redundant ("backup") connection in case of adhesive failure or long-term degradation. An example of such a hybrid system is the São Silvestre footbridge [13-18], which comprises two pultruded GFRP girders adhesively bonded (with epoxy) and bolted to a very thin deck made of steel-fibre reinforced self-compacting concrete (SFRSCC).

Although adhesively bonded connections have been proved to provide virtually full interaction in the short-term, little is known about the durability of such connection systems, namely when subjected to environmental degradation agents, thus raising concerns about their long-term performance. This paper presents experimental and numerical investigations on the durability of adhesively bonded connections between GFRP pultruded profiles and SFRSCC slabs. The main goal was to assess the influence of (i) thermal cycles, likely to be found in outdoor applications, and (ii) wet-dry cycles, on the stiffness and strength of the GFRP-SFRSCC interface. To that end, GFRP-SFRSCC specimens were subjected to thermal and wet-dry cycles for up to 32 weeks and then subjected to push-out tests. Alongside the experimental study, numerical models were developed in order to simulate the push-out tests, in particular to derive (calibrate) time-dependent bond-slip laws representative of the GFRP-SFRSCC connection and of its time-dependent degradation. In the final part of the paper, the effects of the interface degradation on the full-scale structural response of the São Silvestre footbridge are analysed.

2. LITERATURE REVIEW

As mentioned, there are very few studies about the durability and long-term mechanical performance of adhesively bonded connections between pultruded GFRP profiles and concrete members, namely when subjected to thermal and wet-dry cycles. The literature review presented in this section summarizes the main findings reported in previous studies about the durability of (i) the constituent materials and (ii) GFRP-concrete (SFRSCC) interfaces subjected to those environmental agents.

2.1. Constituent materials

2.1.1. Effects of thermal cycles

For the temperature range that is likely to be found in outdoor applications, previous studies have shown that thermal cycles have (very) limited deleterious effects on the mechanical properties of pultruded GFRP materials. Indeed, in spite of the differences between the thermal expansion coefficients of the fibres and the polymer matrix, thermal cycles may even lead to improvements in the material properties due to post-curing effects on the matrix. As an example, Sousa *et al.* [19] subjected pultruded glass-polyester profiles (similar to those used in the present study) to 190 dry thermal cycles between -5ºC and 40ºC. Relatively low changes were measured in the mechanical properties of the GFRP material, with maximum reductions of the longitudinal tensile strength and elasticity modulus of -13.1% and -14.7%, respectively. Grammatikos *et al.* [20] tested similar pultruded glass-polyester profiles exposed to 300 dry and wet (soaked) thermal cycles, between -10ºC and 20ºC. In this case, after dry thermal cycles the longitudinal tensile strength and modulus even increased by 12% and 10%, respectively; in opposition, for wet thermal cycles reductions of respectively -13% and -4% were reported and

attributed to a higher degree of induced microcracking within the matrix material, particularly at the fibre-matrix interface, caused by the additional expansion of the absorbed water during the formation of ice crystals.

Regarding epoxy adhesive, Yagoubi *et al*. [21] subjected epoxy (used in aircraft applications) specimens up to 3000 thermal cycles between -40ºC and 70ºC with relative humidity (*RH*) ranging from ≈0% to 90%, for the lower and higher temperatures, respectively. The authors reported little effects of the accelerated ageing on the mechanical properties of the adhesive, namely on the indentation modulus and the hardness. On the other hand, the same authors reported a decrease in the glass transition temperature (T_g) after 250 cycles, which seemed to stabilize as the ageing process continued. Silva *et al*. [22] tested the tensile properties of the epoxy adhesive used in the current experiments after being subjected to 120 and 240 thermal cycles between -15ºC and 60ºC, each cycle lasting 24h; they reported increases in the strength and elasticity modulus up to 33% and 7%, respectively, after 240 cycles. These results are in accordance with the findings of Moussa *et al.* [23]: the authors heated epoxy adhesives to temperatures slightly above their glass transition temperature (T_g) and then cooled them to ambient temperature; although the epoxy specimens were not subjected to thermal cycles, their strength and stiffness increased and this was attributed to the post curing of the resin.

To the authors' best knowledge there are no studies on the effects of thermal cycles on the mechanical properties of SFRSCC. Unlike polymeric materials, such as GFRP and epoxy adhesives, cementitious materials in general and self-compacting concrete (SCC) in particular do not seem to suffer significant deleterious effects caused by service temperatures [24-26]. In fact, studies on the high temperature behaviour of SCCs indicate

little degradation of their mechanical properties for temperatures up to 100ºC [25,27].

2.1.2. Effects of wet-dry cycles

Thermosetting resins, including polyester (that comprises the matrix of the GFRP profiles used in this study) and epoxy, are susceptible to swelling, plasticization and hydrolysis when subjected to water [28,29]. These physical and chemical degradation phenomena, which can be either reversible or permanent and result from complex reaction/diffusion processes [30,31], are known to cause reductions in their stiffness, strength and toughness related properties [3,21,32].

Borges [33] tested the tensile properties of GFRP pultruded material (similar to that used in this study) in dry state after being subjected to water immersion at 20ºC for up to 24 weeks, obtaining low variations in terms of strength (ranging from -7.3% to -7.5%) and elasticity modulus in tension (+1.1% to -4.5%). The author assessed also the effects of water immersion on the flexural and interlaminar shear properties of the material, and obtained variations of the same order of magnitude. In opposition, Cabral-Fonseca *et al.* [3] reported higher reductions on those mechanical properties, particularly regarding strength (in average -10.6% and -2.7%, for strength and elasticity modulus, respectively) when the same material was subjected to similar ageing conditions but tested in saturated conditions (highlighting the relevance of reversible degradation); in that regard, Quino *et. al.* [32] have shown that particular care must be taken when deriving material properties of wet composites due to non-uniform moisture absorption.

Silva *et al.* [22] subjected specimens of epoxy adhesive (the same used in the current experiments) to 240 and 480 days of immersion in (i) pure water, (ii) salt water (3.5% NaCl) and (iii) wet-dry cycles in salt water (3.5% NaCl), testing their mechanical tensile properties afterwards. The three aging processes had a deleterious effect on the

mechanical response of the specimens with a degradation of the tensile strength ranging from -21% (wet-dry cycles) to -38% (pure water immersion). A similar effect was observed for the elasticity modulus with reductions ranging from -22% (wet-dry cycles) to -47% (pure water immersion). These results show the impact of the deleterious effects of plasticization and hydrolysis phenomena in the mechanical response of these resins.

The exposure of steel fibre reinforced concrete (SFRC) to moisture may lead to fibre corrosion, potentially hindering its durability, a problem that has been addressed by several authors in the last few years. Balouch *et al*. [34] subjected SFRC to salt-fog/dry cycles (1 week wet and 1 week dry during 3 months), showing that for water-to-cement ratios (W/C) under 0.5 (similar to that used in the present study, *cf.* §3), the minimum cover to avoid corrosion of SFRC is under 0.2 mm. Granju *et al*. [35] exposed previously cracked SFRC to salt-fog/dry cycles up to 1 year, reporting light (or no) fibre corrosion for crack widths under 0.5 mm, except for the fibres within the first 2 to 3 mm of the concrete external surface. Furthermore, no deleterious effects were observed in the material strength, which actually increased after the accelerated ageing process, an effect the authors attributed to the roughening of the surface of the lightly corroded steel fibres, thus enhancing their bond to the concrete matrix. This phenomenon was confirmed by Frazão *et al.* [36], who performed fibre pull-out tests on SFRSCC specimens subjected to 10 days of immersion in salt water, reporting an increase of the pull-out strength with the increase of fibre corrosion.

2.2. Pultruded GFRP - concrete interfaces

Although there are several studies on the durability of GFRP-concrete interfaces, they generally focus on GFRP fabrics for externally bonded reinforcement (*e.g*. [37,38]). In

fact, to the authors' best knowledge, only a single study has been reported on the durability of pultruded GFRP-concrete interfaces by Mendes *et al.* [39]. The authors studied the influence of wet-dry cycles in salt-water (at 20-25ºC, 12 h of immersion followed by 12 h of drying per cycle) and thermal cycles (4 h-cycles ranging from -10ºC to 60ºC with target *RHs* of 10% and 80%, respectively) on the epoxy bonded connection between pultruded GFRP profiles and SFRSCC. After 100 cycles in each environment, GFRP-SFRSCC specimens were subjected to static and fatigue push-out tests. The wet-dry cycles in salt water had little influence on the static strength of the connection (a reduction less than 1%); however, unlike what would be expected, the stiffness increased. The thermal-cycles, on the other hand, caused a 32% reduction in strength, as well as a reduction in stiffness. To some extent, the stiffness increase observed in the wet-dry cycles could be attributed to the reduced age of the SFRSCC, which may have further hardened due to the presence of water. However, given the relatively high increase of stiffness, it is possible that this behaviour may have resulted from some anomaly in the measurements of those particular specimens, with further investigations being needed to clarify these results.

2.3. Research significance

The present study aims at contributing to improve the knowledge on the durability of adhesively (epoxy) bonded connections between pultruded GFRP profiles and concrete elements and to clarify some of the questions raised about the previous studies.

To that end, GFRP-SFRSCC epoxy bonded specimens, similar to those tested by Mendes *et al.* [39], were subjected to the effects of both (i) thermal and (ii) wet-dry cycles. The conditions of the first accelerated ageing process were similar to those used by Mendes

et al. [39], ranging from -15ºC to 60ºC with corresponding *RHs* of 0% and 95%, respectively. The duration of each cycle was increased in the present study to 24 h (instead of 4 h) to achieve a better agreement between the target temperature and *RH* curves and those effectively provided by the climatic chamber (*cf.* §3.3.1). In fact, the short duration of each cycle in the previous study might have prevent the specimens to fully reach the target temperatures. Furthermore, the ageing period used previously (100 cycles) was now largely extended in the present investigation (112 to 224 thermal cycles).

Regarding the wet-dry cycles, the present study used fresh (tap) water, which is representative of more service environments than salt water (used in [39]) and known to have a more deleterious effect on polymeric materials [3]. Additionally, the duration of each cycle was increased from 24 h to 2 weeks in order to guarantee a significant water absorption and complete dryness of the specimens in each cycle (*cf.* §3.3.2).

3. EXPERIMENTAL PROGRAMME

3.1. Materials

The experimental tests were carried out using I-shaped GFRP profiles (200×100(×15) mm^2) made of E-glass fibres and an isophthalic polyester resin matrix, produced by *ALTO, Perfis Pultrudidos, Lda*. Small-scale material characterization tests were performed in coupons extracted from the flanges and webs of the GFRP profiles, allowing to determine their main mechanical properties (Table 1): (i) the longitudinal elasticity modulus ($E_{t,L}$) and strength ($f_{tu,L}$) in tension (EN ISO 527 [40]); (ii) the transverse elasticity modulus ($E_{c,T}$) and strength ($f_{cu,T}$) in compression (ASTM D 695 [41]); and

(iii) the in-plane shear modulus (G_{LT}) and strength ($\tau_{u,LT}$) (based on 10º off-axis tensile tests [42]).

The SFRSCC was developed by the company *CiviTest* and incorporated 45 kg/m^3 of hooked end steel fibres with length of 35 mm and diameter of 0.55 mm. The mix composition, comprising a W/C ratio of 0.33, is presented in Table 2. Material characterization tests were performed in SFRSCC cubes and cylinders, at 28 days, allowing the determination of (i) the elasticity modulus ($E_{c,28}$ = 36.97 ± 1.94 GPa) and the Poisson ratio (ν = 0.33 ± 0.03) in compression (LNEC E 397 [43]); (ii) the splitting tensile strength (f_{cr} = 9.42 ± 1.63 MPa, EN 12390-6 [44]); and (iii) the compressive strength (f_{cm} = 80.65 ± 2.07 GPa, EN 12390-3 [45]). Tests were also performed at the age of 905 days, representative of the age of the SFRSCC when the push-out tests were performed: E_c = 40.88 ± 1.53 GPa; f_{cr} = 11.19 ± 1.08 MPa; and f_{cm} = 93.01 ± 7.42 GPa.

The adhesive connection between the GFRP and the SFRSCC was provided by an epoxy adhesive, *S&P Resin 220* [46], which was thoroughly characterized by Silva *et al*. [22], namely regarding its elasticity modulus (E_a = 7.15 ± 0.27 GPa) and strength (f_{au} = 22.0 ± 1.0 MPa) in tension. Firmo *et. al*. [47] reported a glass transition temperature (T_g) for this adhesive of 47ºC (based on the onset of the storage modulus decay from DMA tests in a dual cantilever setup) while Roquette [48] reported a shear strength of (τ_{au}) 25.1 ± 1.5 MPa and a shear modulus (G_a) of 4.61 ± 0.57 MPa, obtained from V-notch beam tests.

3.2. Geometry and preparation of test specimens

The experimental programme comprised push-out tests in GFRP-SFRSCC specimens made of a pultruded GFRP profile segment connected with epoxy adhesive to two

SFRSCC slabs. The geometry of the specimens (Figure 1) followed the recommendations provided in Annex B of Eurocode 4 [49].

The preparation of the specimens began with the roughening of the SFRSCC surfaces, using a needle scaler (as shown in Figure 2a), in order to enhance the quality of the adhesive bonding. The morphology of the SFRSCC surface was not measured; however, in a previous study [50] conducted in similar slabs made of concrete type MC (0.40) (according to EN 1766 [51]), the same surface preparation procedure led to a surface roughness index of 0.164 mm, according to the sand test described in [51]. The SFRSCC surfaces were then dusted with compressed air and the GFRP surfaces were cleaned with acetone. The epoxy adhesive was prepared according to the manufacturer's recommendations [46] and applied to the SFRSCC surface, as depicted in Figure 2b. The GFRP profiles were positioned on the top of the slab and a weight was placed over them in order to squeeze the excessive adhesive, which was then removed. The 2 mm epoxy adhesive layer was guaranteed by gluing small plastic spacers onto the GFRP flanges. After a 24-hour period defined for the epoxy adhesive to set, the process was repeated in order to connect the second SFRSCC slab to the specimens, as shown in Figure 2c.

3.3. Ageing processes and test series

Table 3 lists the number of specimens subjected to each ageing process and exposure period, as well as the experimental results for each series, discussed in the following sections. In total, 16 specimens were subjected to thermal cycles and 9 specimens were subjected to wet-dry cycles. Before being subjected to the ageing processes, specimens were kept in the laboratory environment (average temperature of ~20ºC, not controlled) for a period of 1 month, to guarantee the curing of the adhesive. After removal from the

ageing chambers, specimens were stored in the laboratory environment for a minimum period of 1 month to guarantee that they were tested in a dry state. In addition, as a reference, 4 control specimens were also kept in the laboratory environment for a period of 1 month, to guarantee the curing of the adhesive, before being tested.

3.3.1. Thermal cycles

The thermal cycles were defined based on EN 13687-3 [52] standard. For each 24-hour cycle, temperatures ranged from -15ºC to 60ºC (Figure 3), while the *RH* was planned to vary from 0% to 95% (Figure 4). This ageing process was conducted in a climate chamber, from *Aralab*, model *Fitoclima 6400*. Although the temperature protocol was fairly well reproduced (*cf*. Figure 3), the climate chamber was not able to follow the target *RH* curve - as shown in Figure 4, the RH ranged from ~10% to ~50-60%.

It is worth noting that there are no standardized protocols for testing GFRP-concrete connection systems, nor any requirements in the literature for the number of cycles to be performed. Existing standards for other construction materials or systems define the number of thermal cycles, which typically range from 5 to 50. Given that GFRP based structures are generally designed for relatively long service life periods (between 50 and 100 years), the maximum number of thermal cycles was set as 200.

3.3.2. Wet-dry cycles

The wet-dry cycles were performed using a large scale wet chamber (often used to cure concrete specimens), which permanently maintained the *RH* over 95%. Each cycle lasted two weeks, with specimens remaining inside the wet chamber (set at 20ºC) for one week and outside the chamber (in the laboratory indoor dry environment at ~20ºC and RH varying from 50% to 65% (not monitored) for the remaining week. As for the thermal

cycles, there are no specific test protocols defining the maximum number or duration of wet-dry cycles for GFRP-concrete connection systems. On one hand, the duration of the cycles was defined to achieve a significant level of water absorption. Recent studies have shown that for water immersion at 20ºC, the weight change of an epoxy adhesive (similar to that used in this study) is around 1.0% after 1 week, whereas the saturation level (after over 250 weeks) is around 2.1% [53,54]. Thereafter, an exposure period of 168 h (wet part of the cycle) was deemed as sufficient to induce significant water absorption on the adhesive of the push-out specimen. On the other hand, in order to enable a comparison of the effects of the wet-dry and thermal cycles, it was decided that the ageing period of the wet-dry cycles should match that of the thermal cycles.

3.4. Procedure and instrumentation of push-out tests

Figure 5 shows the setup used in the push-out tests. The load was applied to the specimens with a hydraulic press from *Enerpac*, with a capacity of 3000 kN. Specimens were placed on the bottom (moving) plate of the press over a thin plaster embedment. The load was measured with a load cell from *Microtest*, with a capacity of 3000 kN. A sphere was placed in-between the load cell and the top plate allowing the rotation of the latter. The relative displacements between the bottom and top surfaces of the specimens were measured with four displacement transducers from *TML*, with a stroke of 25 mm and precision of 0.01 mm. One displacement transducer was placed on the bottom plate, while the three remaining ones were placed on the top plate (to detect eventual rotations).

In order to reduce the deformations resulting from the settlement of the test setup (not related with the bonding mechanism under study), the specimens were first subjected to a loading/unloading cycle up to approximately 10% of their expected failure load, which was determined based on preliminary tests [13]. The specimens were then monotonically

loaded up to failure, under displacement control of the bottom test plate, at a rate of approximately 0.5 mm/min.

4. EXPERIMENTAL RESULTS

Figure 6 depicts the load-relative displacement (between the top and bottom surfaces of the specimens) curves obtained for a representative specimen from each series and exposure period. In addition to the average failure load (F_u) and stiffness (K) for each series, the results obtained for all specimens are summarized in Table 3. It should be mentioned that the stiffness (K) was computed by the slope of the load-relative displacement curves, within their linear branch, typically between 200 kN and 250 kN. Note that such displacement curves account for the interface slip and the axial deformation of the GFRP profile and SFRSCC slabs. The influence of the latter deformation on the overall relative displacement is estimated to range between 9% and 21%, for the experimental series with lower and higher stiffness (*cf.* Table 3), respectively.

Before testing, all specimens subjected to wet-dry cycles presented exterior signs of ageing, namely scattered corrosion of exposed steel fibres. On the other hand, for the thermal cycles exposure, these signs of damage were only visible in specimens subjected to 224 cycles. Regarding the load-relative displacement behaviour, specimens of all series presented an initial linear behaviour up to a peak load, which corresponded to the failure initiation of the GFRP-SFRSCC interfaces. The values of the stiffness and of the peak load were the most significant differences observed in these curves (*cf.* Figure 6).

Three different governing failure modes were observed (Table 3), two at the GFRP-SFRSCC connection: (i) cohesive failure on the SFRSCC (a thin layer of concrete in contact with the adhesive, hereon simply referred to as cohesive, *cf.* Figure 7a); and

(ii) adhesive failure at the interface between the epoxy adhesive and the GFRP (from now on referred to as adhesive, *cf*. Figure 7b). A third failure mode was observed, caused by the rupture of the web-flange junction of the profiles (*cf*. Figure 7c). Furthermore, for some specimens, after the occurrence of the first failure mode (in one of the sides of the specimen), a second failure mode was observed, typically on the opposite side, leading to the collapse of the specimens.

Specimens of the control series presented the general behavior discussed earlier, exhibiting cohesive failure of the interface (on the SFRSCC material, Figure 7a) followed by web-flange junction rupture on the opposite side (Figure 7b).

4.1. Influence of thermal cycles

All specimens subjected to 112 thermal cycles (Th-t1) failed due to the cohesive failure of the GFRP-SFRSCC interface (Figure 7a). Specimens of series Th-t2 (168 thermal cycles) failed also due to cohesive debonding at the interface (Figure 7a), with one of the specimens (Th-t2-2) presenting web-flange junction rupture (on the opposite side) as secondary failure mode (Figure 7c). Finally, specimens subjected to 224 thermal cycles (Th-t3) presented visible debonding on both interfaces and failed due to the complete debonding at one of the sides, with the exception of specimen Th-t3-5, which presented complete debonding at both interfaces. Unlike the previous series, the (mainly) cohesive failure presented localized debonding patches in the epoxy adhesive itself.

Figures 8 and 9 show the evolution of the ultimate load and of the stiffness, respectively, with the number/duration of thermal cycles, together with the numerical results to be discussed later. It can be seen that the ultimate load presented a slightly increasing general trend with the number of thermal cycles, with a strength increase of 19% at the end of

exposure period. Most likely this increasing trend, which contrasts with the reduction reported by Mendes *et al*. [39] after 100 cycles, is due to the post-curing effect of the thermal cycles on the epoxy resin. The difference between these results may be related to the different ages of the SFRSCC used in the experiments (under 5 months for Mendes *et al*. [39] and over 3 years in the present study); indeed, younger SFRSCC may be more prone to deleterious effects under exposure to thermal cycles. In opposition, the thermal cycles caused a general decrease of the average stiffness (consistent with the data reported by Mendes *et al*. [39]), which was particularly steep for the last exposure period, with a reduction of -48% after 224 cycles. The remarkable stiffness reduction observed from 168 to 224 cycles is consistent with the damage observed in specimens from series Th-t3, in which failure was not exclusively cohesive on the SFRSCC, with failure patches being easily identified on the epoxy adhesive. This seems to indicate that the cumulative effects of the thermal cycles were the cause of such debonding patches at the interface, possibly due to thermal fatigue owing to the internal stresses associated with the different coefficients of thermal expansion (CTE) of the materials involved. In fact, for concrete a CTE of 10×10^{-6}/ºC is generally assumed [55], Klamer [56] reports a CTE of 26×10^{6}/ºC for a similar epoxy adhesive, while for GFRP CTEs of 6.7×10^{-6}/ºC and 22×10^{6}/ºC for the longitudinal and transverse directions, respectively, have been reported [57,58]. It is worth mentioning that the interface failure is generally governed by shear and peeling stress peaks, which usually develop at the extremities of the connection, with the bonded interface being able to present some stress redistribution. This may explain why those failure patches in the adhesive affected the stiffness but yet did not cause a strength reduction (further discussion on this aspect is provided in Section 5).

4.2. Influence of wet-dry cycles

Specimens subjected to 8 wet-dry cycles (WD-t1) failed due to the debonding of the GFRP-SFRSCC interface. Failure was observed mainly in the epoxy adhesive, although cohesive failure patches were also identified (Figure 7b). Unlike the previous series, all specimens subjected to 12 wet-dry cycles (WD-t2) presented different failure modes: (i) WD-t2-1 failed at both web-flange junctions (Figure 7c), although it also presented signs of debonding at the top of one of the interfaces; (ii) WD-t2-2 presented web-flange junction failure at one of the sides of the specimen, which was followed by the complete adhesive debonding of the interface on the other side; and (iii) WD-t2-3 failed due to the complete debonding of one of the GFRP-SFRSCC interfaces. Again, the debonding of the last two specimens was observed mainly in the epoxy adhesive (Figure 7b), although cohesive failure patches were also identified. Regarding specimens aged with 16 wet-dry cycles (WD-t3), for two of the specimens the first failure mode was the rupture of the web-flange junction (Figure 7c), which was followed by the adhesive debonding of the interface on the opposite side; the remaining specimen failed due to the complete debonding of one of the interfaces. In both cases, the debonding occurred mainly in the adhesive with patches of cohesive failure (Figure 7b).

For the specimens that presented web-flange junction failure as the primary or unique failure mode it should be mentioned that it was not always possible to determine the level of damage (if any) on the interface prior to failure, although it is very likely to have occurred.

Figures 10 and 11 show the evolution of the ultimate load and of the stiffness, respectively, with the number/duration of wet-dry cycles, together with numerical results to be discussed later. The results obtained indicate that the wet-dry cycles did not influence the strength of

the GFRP-SFRSCC connection – the relative variations for all cycles are very small (maximum of 5%), well within the experimental scatter. On the other hand, the stiffness of the GFRP-SFRSCC connection was very significantly affected by this type of ageing, with reductions from -53% already after 8 cycles to -58% after 16 cycles. This degradation occurred mostly during the earlier stages of the exposure period (before 16 weeks) and then tended to stabilize. Therefore, it seems that the degradation was mostly caused by the water absorption of the epoxy adhesive (Cabral-Fonseca [59] reported a water absorption of 1.03% for a similar adhesive at 23ºC) and the GFRP profile (*cf.* §3.3.2) and the consequent plasticization and hydrolysis phenomena underwent by their polymeric constituents (*cf.* §2.1.2), and not by the wetting and drying cycles *per se*. In spite of such significant stiffness decrease, as mentioned the strength was not significantly affected; this is attributed to the effect of ageing on the adhesive, which became softer and therefore led to a smoother stress distribution at the interface; further discussion is provided in the numerical analysis (*cf.* §5.2).

The above mentioned influence of wet dry cycles in interfacial strength is consistent with the data presented by Mendes *et al*. [39], who also reported no strength degradation due to this type of exposure; however, in their study, the stiffness of aged specimens exhibited an unexpected increase – our results present and opposite (and logical) trend, which seems to confirm that the stiffness data obtained in that study were somehow anomalous.

5. NUMERICAL SIMULATION

5.1. Objectives and model description

The numerical study comprised the development of three-dimensional finite element (FE) models of the push-out tests. The objectives were two-fold: (i) to improve the

understanding about the mechanical behaviour of adhesively bonded connections between GFRP profiles and SFRSCC elements; and (ii) to assess the feasibility of using bond-slip laws (Figure 12) to numerically simulate the behaviour of those bonded connections and of their environmental degradation. Those laws were calibrated based on the load-relative displacement behaviour observed in the experimental tests, and aimed at predicting the failure load and the most typical failure mode observed.

The FE models of the push-out tests were developed with the commercial package ABAQUS [60]. In order to reduce the computational costs, only a quarter of the specimens was modelled using symmetry boundary conditions (Figure 13). The models comprised 4 sets of elements: (i) the GFRP profile and (ii) the SFRSCC, which were modelled with 8-node brick elements (C3D8), with three degrees of freedom per node (translations); (iii) the joint GFRP/SFRSCC interface was modelled by means of a stiffness uncoupled bi-linear bond-slip law (*cf*. Figure 12); and (iv) boundary linear springs, in the vertical direction (Y, *cf*. Figure 1), which simulated the contact between the bottom surface of the SFRSCC slab and the plaster layer over the press plate (these springs were adopted in order to avoid the influence of the initial setting of the specimens in the calibration of the aforementioned slip law, in particular on its stiffness). Generally, a regular mesh was adopted with 5 mm side cubic elements. Near the interface, in the SFRSCC slab and in the GFRP flange, the mesh was refined in the through-thickness direction, by adopting a 1 mm size followed by two consecutive 2 mm layers. The analyses were performed by applying an imposed vertical deformation at the top surface of the GFRP profile.

The materials were modelled with the elastic and strength properties derived from testing (*cf*. §3.1). The elastic constant introduced in the models are given in Table 5, where 1, 2 and 3 stand for the longitudinal, transverse and through-thickness direction. For the

SFRSCC, given its isotropic nature, only one elasticity modulus (E_1) and Poisson ratio (υ_{12}) are given. The GFRP was modelled as orthotropic and with linear-elastic behaviour. For the SFRSCC, the *Concrete Damaged Plasticity* built-in material model was adopted, considering a 30º dilatation angle. In compression, the SFRSCC behaviour was considered perfectly plastic at f_{cm} (80.65 MPa, although this stress level was never reached), while in tension the behaviour was considered elastic up to f_{cr} (9.42 MPa) with brittle failure, thereafter. This definition of damage behaviour did not result from an experimental characterization of the fracture behaviour of the SFRSCC; however, as discussed in the next section, the models presented only residual concrete damage levels (in accordance with the experimental results) and, therefore, the damage model was not relevant for the analysis and the calibration of its parameters for the SFRSCC, particularly the introduction of a tensile fracture energy, was not pursued. The properties of the GFRP and SFRSCC materials were considered to be unaffected by the ageing processes owing to the relatively small degradation of those individual materials reported in the literature (*cf.* §2.1) for the type of ageing used in the experiments. In other words, in the numerical analysis only the degradation of the interface was considered, by changing the parameters of the bond-slip law (as explained below). With this respect, it should be mentioned that concentrating the aging effects in the bond-slip law, any local degradation of the substrates – the GFRP and the SFRSCC – is reflected on the parameters of those laws, albeit this method does not differentiate the failure modes within the interface (*i.e.* adhesive or cohesive).

To calibrate the stiffness of the linear springs simulating the contact between the SFRSCC and the plaster layer a preliminary linear-elastic model of the Control series was developed, where the epoxy adhesive layer at the interface was explicitly modelled with four layers of solid elements (C3D8). For these elements, a regular mesh was also adopted

(5×5×0.5 mm^3). The stiffness of the equivalent area spring governing the SFRSCC-plaster interface was set as 39270 (kN/mm)/m^2, which was used in the remaining models (*i.e.*, those in which the interface was modelled with a bond-slip law).

For the sake of simplicity, and given the limited data retrieved from the experimental tests, the bi-linear bond-slip laws were calibrated considering the same behaviour on the three relevant directions, *i.e*. in the normal direction (mode I – direction *n*) and in the two orthogonal tangential directions (mode II – direction t_1; mode III – direction t_2). In this regard, it should be mentioned that, due to the test setup, the response of the specimens is governed by the in-plane shear XY response (mode II) – *cf.* Figure 1. This was confirmed by testing also bi-linear laws in which the maximum normal interfacial stress (σ_{max}) was much higher (>150 times) than the maximum tangential interfacial stress (τ_{max}). The results obtained with both sets of laws are coincident except for the very last stages of the post-peak behaviour (not very relevant in these analyses), showing deviations under 3% in force, thus validating the simplifying assumption considered. The failure initiation criterion was the maximum nominal stress in each direction, following Eq. (1).

$$\max\left\{\frac{\langle\sigma\rangle}{\sigma_{max}}, \quad \frac{\tau_1}{\tau_{max}}, \quad \frac{\tau_2}{\tau_{max}}\right\} \leq 1.0 \tag{1}$$

where, σ, τ_1 and τ_2 are the normal (direction *n*) and shear (directions t_1 and t_2) stresses at the interface, respectively, $\langle\,\rangle$ represents the Macaulay bracket and σ_{max} and τ_{max} are the normal and shear "pure" strengths (*cf.* Figure 12). The damage evolution then follows the bi-linear bond-slip law (*cf.* Figure 12), with stresses being expressed as follows,

$$\sigma = \begin{cases} (1-D)\bar{\sigma}, & \bar{\sigma} \geq 0 \\ \bar{\sigma}, & \bar{\sigma} < 0 \end{cases} \quad \tau_1 = (1-D)\bar{\tau}_1 \quad \tau_2 = (1-D)\bar{\tau}_2 \tag{2a), (2b) and (2c)}$$

where, $\bar{\sigma}$, $\bar{\tau}_1$and $\bar{\tau}_2$ are the normal and shear (directions t_1 and t_2) stresses at the interface predicted without damage and D is the scalar damage variable (automatically computed by

the software during the analysis), given by Eq. (3).

$$D = \frac{d_u^m (d_{max}^m - d_{cr}^m)}{d_{max}^m (d_u^m - d_{cr}^m)} \tag{3}$$

where, d_u is the ultimate slip, d_{cr} is the critical slip ($d_{cr} = (\tau_{max}\ or\ \sigma_{max})/k$, *cf.* Figure 12) and d_{max} is the maximum slip during the loading history (to avoid healing). The superscript m denotes the effective slip under combined normal and shear stresses, expressed in Eq. (4).

$$d_m = \sqrt{\langle d_n \rangle^2 + d_{t_1}^2 + d_{t_2}^2} \tag{4}$$

where, d_n, d_{t_1} and d_{t_2} represent the separation under normal (direction *n*) and shear (directions t_1 and t_2) stresses, respectively.

Thereafter, the calibration was performed in a sequential process. The interface stiffness was initially calibrated by adjusting the parameter *k*. Next, parameters τ_{max} and σ_{max}, which, together with the softening slip[1] (d_{soft}, for modes II and III), representing the difference between the ultimate slip (d_u) and the critical slip (d_{cr}), govern the strength of the interface, were adjusted in order to obtain ultimate loads (F_u) similar to those measured in the experiments. It should be mentioned that the latter parameter (d_{soft}) was adjusted for the Control series, providing a similar post-peak behaviour to that observed in the experiments and maintained constant (at 0.5 mm) for the remaining series (as they presented a similar post-peak behaviour). In this regard, it shoud be mentioned that d_{soft} is the main parameter governing the post-peak behaviour, which was a less relevant concern for the present numerical analysis; in the experiments, that stage of the behaviour may have been influenced by the existence of two interfaces per specimen and the inherent

[1] For mode I, such displacement corresponds to the opening of the interface.

asymmetries caused by their non-simultaneous failure initiation and propagation. The simplifying assumption of a constant d_{soft} parameter allowed for a direct comparison of the maximum strength parameters (τ_{max} and σ_{max}) between the different series. The stiffness and strength parameters were calibrated with minimum steps of 0.5 MPa/mm and 0.5 MPa, respectively. For each case, the iteration that presented the lowest deviations between experimental and numerical results regarding failure load (F_u) and global stiffness (K) was chosen, with minimum relative difference of ~5% being considered acceptable for the calibration procedure.

The possibility of occurrence of damage initiation in the GFRP material was also assessed by computing the Tsai-Hill failure initiation index, which may be expressed as follows for plane stress elements [61],

$$\frac{\sigma_1^2}{X^2} - \frac{\sigma_1 \sigma_2}{X^2} + \frac{\sigma_2^2}{Y^2} + \frac{\tau_{12}^2}{S^2} \leq 1.0 \quad (5)$$

where, σ_1 and σ_2 are the stresses in the principal directions 1 and 2, respectively, τ_{12} is the shear stress in the plane defined by those directions, X and Y are the strengths in the principal directions and S is the in-plane shear strength. Applying Eq. (5) to the present case study, the principal directions 1 and 2 may be taken as the longitudinal and transverse directions, replacing σ_1, σ_2 and τ_{12} by σ_L, σ_T and τ_{LT}, respectively, and X, Y and S by $f_{tu,L}$, $f_{cu,T}$ and $\tau_{u,LT}$, respectively (*cf.* Table 1).

5.2. Results

Table 4 summarizes the parameters of the bond-slip laws calibrated for each series and the corresponding numerical results, as well as the comparison with the experimental counterparts, while Figures 14 and 15 illustrate the evolution of the calibration parameters. Numerical and experimental results are in very good agreement, with maximum relative

differences of 5.4% regarding the ultimate load and 5.7% regarding the stiffness, well within the experimental scatter (*cf.* Figures 8 and 9 for the thermal cycles, and Figures 10 and 11 for the wet-dry cycles series).

Figures 16 and 17 compare for the thermal and wet-cry cycles, respectively, the experimental load-relative displacement curves representative of each series with those retrieved by the FE models. For the experimental curves presented in these Figures, it should be noted that, unlike the curves presented in Figure 6, the initial non-linear behaviour, attributed to the settlement of the specimens, was linearized in order to provide a more meaningful comparison with the numerical results. Again, a general good agreement is obtained.

Concerning the failure modes, for all durations and types of exposure the FE models predicted failure to occur at the interface. This is also consistent with the experiments, as failure generally started at the interface. Figures 18 and 19 plot the numerical load-relative displacement curves together with the evolution of the (maximum value of the) Tsai-Hill failure initiation index at the web-flange junction, for the thermal and wet-dry cycles series, respectively. These figures show that for all series the peak loads (F_u), corresponding to failure initiation, occurred when the Tsai-Hill failure initiation indexes were lower than 1.0, confirming that in general failure started at the interface and not in the GFRP profiles. After the peak loads are attained, the stiffer models (for Control, Th-t1 and Th-t2 series) presented a softening stage and the Tsai-Hill failure initiation indexes considerably increase, exceeding 1.0, which is also consistent with the experimental observations, namely regarding the failure in the web-flange junction of the GFRP profile that followed the interfacial failure. Moreover, these results indicate that the specimens that presented the first failure at the web-flange junction (WD-t2 and WD-t3 series) are likely to have suffered (undetected) damage at the

interface before such failure occurred, as suggested earlier (*cf.* §4.3)

Regarding the SFRSCC, although some tensile damage was locally observed in the models, as exemplified by Figure 20 for the control series, its value was very low (< 0.02 in a scale from 0 to 1). In fact, if the SFRSCC is considered linear-elastic the load-relative displacement curves match those obtained considering the plasticity model. In other words, even following a conservative approach in the definition of fracture properties, this material is largely kept within its elastic branch of behaviour, both in tension and compression.

Another interesting result derived from the models is the evolution of the shear stress distribution along the interface. Figure 21 compares the shear stress distribution at the interface obtained with the calibration parameters of the Control series to those obtained with the calibration parameters of the least stiff series Th-t3 and WD-t3. In the aged series, the steep reduction of the interfacial stiffness led to an almost uniform shear stress distribution along the interface, considerably reducing the stress peak values that occur in the Control series. Such a smoother shear stress distribution has contributed to delay the failure triggering in the aged series, explaining why the failure load did not decrease in both aged experimental series. Additionally, it is interesting to notice that, in the transverse direction, the shear stresses are higher at the side of the GFRP web (right hand side of the models in Figure 21), indicating that the added out-of-plane stiffness provided by the web allows the development of higher in-plane (shear) stresses.

6. EFFECTS OF AGEING ON THE STRUCTURAL PERFORMANCE

The experimental results have shown that both types of ageing have a deleterious effect on the stiffness of the GFRP-SFRSCC bonded interface. Since the design of GFRP based structures is often governed by serviceability requirements (deflection limits), it seems

relevant to assess the influence of the interface degradation on the overall deformations of hybrid structural members. As discussed in [10], these deformations comprise the contribution of both bending and shear deformations, making it necessary to use Timoshenko beam theory (instead of Euler-Bernoulli beam theory). Regarding the contribution of shear to the overall deformation of GFRP-concrete hybrid beams, as discussed in [10,17,18], the shear stiffness is largely governed by the GFRP webs.

In what concerns the contribution of bending to the deformation of a simply supported hybrid beam, the ratio between the midspan deflection considering full (δ_f) and partial (δ_p) shear interaction is given by Eq. (6) [62],

$$\frac{\delta_p}{\delta_f} = 1 + \left(\frac{EI_{comp}}{\sum EI_{part}} - 1\right) \times \beta \tag{6}$$

where, EI_{comp} is the flexural stiffness of the hybrid beam, EI_{part} is the individual flexural stiffness of each component (in this case, GFRP and SFRSCC) and β is a non-dimensional stiffness parameter given by,

$$\beta = \left[\frac{1}{\cosh\left(\frac{\alpha L}{2}\right)} + \frac{1}{8}(\alpha L)^2 - 1\right] \times \frac{384}{5(\alpha L)^4} \tag{7}$$

and

$$\alpha = K\left[\sum\left(\frac{1}{EI_{part}}\right) + \frac{r^2}{\sum EI_{part}}\right] \tag{8}$$

where, L is the span of the structure, K is the shear stiffness of the connection and r is the distance between the neutral axis of each component of the section.

Thereafter, in order to assess the structural consequences of the interfacial stiffness degradation, the above-mentioned formulae were applied to the São Silvestre footbridge (*cf.* Figure 22), a 10.5 m span simply supported hybrid bridge comprising two GFRP girders (I400×200×15 mm^2) and a very thin SFRSCC deck (37.5 mm thick, 2000 mm wide)

connected by a 2 mm epoxy adhesive layer [18]. The stiffness of the interface was taken directly from the tests[2], since the adhesive area is the same: 2 (flanges) × (100×2) mm^2 in the push-out specimens and 200×2 mm^2 per girder of the bridge. Figure 23 presents the variation of the (δ_p/δ_f) ratio with the interface stiffness, indicating the ratio for the average stiffness obtained in each series of the experimental tests. The results show that although there is a considerable reduction in the shear connection stiffness (up to ~60%), the effects at the full-scale structural level of the ageing processes are not significant, causing a maximum increase of only 5% in the predicted flexural elastic deflection, as predicted using Eq. (6).

7. CONCLUSIONS

This paper presented an experimental and numerical study about the mechanical behaviour of adhesively bonded connections between GFRP pultruded profiles and SFRSCC slabs subjected to two accelerated ageing protocols: (i) thermal cycles and (ii) wet-dry cycles.

For the test conditions used in the study, the thermal cycles did not have a deleterious effect on the interfacial strength; in fact, after 224 cycles, the strength increased by 19%. On the other hand, the stiffness presented a significant reduction of -48%.

The wet-dry cycles did not affect the strength of the interface, which presented marginal variations during the exposure period. Yet, as for the thermal cycles, the stiffness was markedly affected, presenting a sharp reduction already for the earlier periods of ageing,

[2] As mentioned earlier (*cf.* §4), the stiffness measured in the experiments also accounts for the axial deformability of the GFRP and SFRSCC (contribution to overall deformability ranging from 9% to 21%). Using these values in the present analysis is a conservative simplifying assumption with reduced influence in the final results.

with a maximum stiffness reduction of -58% after 16 cycles.

In the numerical study, bi-linear bond-slip laws representative of the changes underwent by the bonded interfaces were calibrated. The models were able to capture the mechanical responses observed in the experiments, including the effects of the accelerated ageing – the models accurately predicted the load *vs*. relative displacement responses and also the failure mechanisms. The models also showed that for lower interface stiffness the shear stress distribution is more uniform and the stress peaks are lower, which to some extent explains why the interfacial strength did not decrease in the push-out experiments.

In the final part of the paper, the consequences of the interface stiffness degradation were assessed at the full-scale structural level. To that purpose, taking the São Silvestre footbridge as an example, it was concluded that the very significant bond stiffness reduction causes an increase of the mid-span elastic deflection of only 5%. This means that although thermal and wet-dry cycles considerably reduce the stiffness of the GFRP-epoxy-SFRSCC interface, this does not seem to significantly influence the structural safety at service limit states.

8. ACKNOWLEDGEMENTS

This work was developed in the frame of research projects *PONTALUMIS* (funded by ANI, project 2009/003456) and RAISE (funded by FCT, project PTDC/ECM-EST/2701/2014). The authors would like to acknowledge CERIS, ISISE, FCT and ANI for the financial support, ALTO Perfis Pultrudidos, Lda. for supplying the GFRP pultruded profiles, and SIKA, S&P and INTEC for supplying the other materials used in the experiments. The first author is also grateful to FCT for funding his research through scholarship SFRH/BPD/112216/2015.

9. REFERENCES

[1] Correia JR. *GFRP Pultruded Profiles in Civil Engineering: Hybrid Solutions, Bonded Connections and Fire Behaviour*, PhD Thesis in Civil Engineering, Instituto Superior Técnico, Technical University of Lisbon; 2008.

[2] Liao K, Schultheisz CR, Hunston DL. Effects of environmental aging on the properties of pultruded GFRP. *Composites Part B: Engineering* 1999; 30(5): 485-493.

[3] Cabral-Fonseca S, Correia JR, Rodrigues MP, Branco FA. Artificial accelerated ageing of GFRP pultruded profiles made of polyester and vinylester resins: characterization of physical-chemical and mechanical damage. *Strain* 2012; 48(2): 162-173.

[4] Mara V, Haghani R, Harrysin P. Bridge decks of fibre reinforced polymer (FRP): A sustainable solution. *Construction and Building Materials* 2014; 50: 190-199.

[5] Deskovic N, Triantafillou T, Meier U. Innovative design of FRP combined with concrete: Short-term behaviour. *Journal of Structural Engineering* 1995; 121(7): 1069-1078.

[6] Hall JE, Mottram JT. Combined FRP reinforcement and permanent formwork for concrete members. *Journal of Composites for Construction* 1998; 2(2): 78-86.

[7] Fam AZ, Rizkalla SH. Flexural behavior of concrete-filled fiber-reinforced polymer circular tubes. *Journal of Composites for Construction* 2002; 6(2): 123-131.

[8] Hulatt J, Hollaway L, Thorne AM. The use of advanced composites to form an economic structural unit. *Construction and Building Materials* 2003; 17(1): 55-68.

[9] Keller T, Schaumann E, Vallée T. Flexural behavior of a hybrid FRP and lightweight concrete sandwich bridge deck. *Composites Part A: Applied Science and Manufacturing* 2007; 38(3): 879-889.

[10] Correia JR, Branco FA, Ferreira JG. Flexural behaviour of GFRP–concrete hybrid beams with interconnection slip. *Composite Structures* 2007; 77(1): 66-78.

[11] Correia JR, Branco FA, Ferreira JG. GFRP-concrete hybrid cross-sections for floors of buildings. *Engineering Structures* 2009; 31(6): 1331-1343.

[12] Correia JR, Branco FA, Ferreira JG. Flexural behaviour of multi-span GFRP-concrete hybrid beams. *Engineering Structures* 2009; 31(7): 1369-1381.

[13] Gonilha JG. *GFRP-concrete hybrid structural systems. Application to the development of a footbridge prototype*, PhD Thesis in Civil Engineering, Instituto Superior Técnico, University of Lisbon; 2014.

[14] Gonilha JA, Correia JR, Branco FA. Dynamic response under pedestrian load of a GFRP-SFRSCC hybrid footbridge prototype: Experimental tests and numerical simulation. *Composite Structures* 2013; 95: 453-463.

[15] Gonilha JA, Correia JR, Branco FA. Creep response of GFRP–concrete hybrid structures: application to a footbridge prototype. *Composites: Part B* 2013; 53: 193-206.

[16] Gonilha JA, Correia JR, Branco FA, Caetano E, Cunha A. Modal identification of a GFRP-concrete hybrid footbridge prototype: experimental tests and analytical and numerical simulations. *Composite Structures* 2013; 106: 724-733.

[17] Gonilha JA, Correia JR, Branco FA. Structural behaviour of a GFRP-concrete hybrid footbridge prototype: Experimental tests and numerical and analytical simulations. *Engineering Structures* 2014; 60: 11-22.

[18] Gonilha JA, Barros J, Correia JR, Sena-Cruz J, Branco FA, Ramos LF, Gonçalves D, Alvim MR, Santos T. Static, dynamic and creep behaviour of a full-scale GFRP-SFRSCC hybrid footbridge. *Composite Structures* 2014; 118: 496-509.

[19] Sousa JM, Correia JR, Cabral-Fonseca S, Diogo AC. Effects of thermal cycles on the mechanical response of pultruded GFRP profiles used in civil engineering applications. *Composite Structures*, 2014; 116: 720-731.

[20] Grammatikos SA, Jones RG, Evernden M, Correia JR. Thermal cycling effects on the durability of a pultruded GFRP material for off-shore civil engineering structures. *Composite Structures*, 2016; 153: 297–310.

[21] Yagoubi JE, Lubineau G, Shahid S, Verdue J, Askari A. Thermomechanical and hygroelastic properties of an epoxy system under humid and cold-warm cycling conditions. *Polymer Degradation and Stability*, 2014; 99:146-155.

[22] Silva P, Fernandes P, Sena-Cruz J, Xavier J, Castro F, Soares D, Carneiro V. Effects of different environmental conditions on the mechanical characteristics of a structural epoxy. *Composites Part B*, 2016; 88:55-63.

[23] Moussa O, Vassilopoulos AP, Castro J, Keller T. Time-temperature dependence of thermomechanical recovery of cold- curing structural adhesives. *International Journal of Adhesion and Adhesives*, 2012; 35:94-101.

[24] Khoury GA. Compressive strength of concrete at high temperatures: a reassessment. *Magazine of Concrete Research*, 1992; 44(161): 291-309.

[25] Pineauda A, Pimienta P, Rémond S, Carré H. Mechanical properties of high performance self-compacting concretes at room and high temperature. *Construction and Building Materials*, 2016; 112: 747–755.

[26] Fares H, Noumowe A, Rémond S. Self-consolidating concrete subjected to high temperature: Mechanical and physicochemical properties. *Cement and Concrete Research*, 2009; 39(12): 1230–1238.

[27] Khaliq W, Kodur V. Thermal and mechanical properties of fiber reinforced high performance self-consolidating concrete at elevated temperatures. Cement and Concrete Research, 2011; 41: 1112–1122.

[28] Zhou J, Lucas JP. Hygrothermal effects of epoxy resin. Part I: the nature of water in

epoxy. *Polymer*, 1999; 40(20): 5505–5512.

[29] Lee MC, Peppas NA. Water Transport in Epoxy Resins. *Progress in Polymer Science*, 1993; 18(5): 947-961.

[30] Yagoubi JE, Lubineau G, Roger F, Verdu J. A fully coupled diffusion-reaction scheme for moisture sorption-desorption in an anhydride-cured epoxy resin. *Polymer*, 2012, 53(24): 5582-5595.

[31] Yagoubi JE, Lubineau G, Traidia A, Verdu J. Monitoring and simulations of hydrolysis in epoxy matrix composites during hygrothermal aging. *Composites Part A: Applied Science and Manufacturing*, 2015, 68: 184-192.

[32] Quino G, Yagoubi JE, Lubineau G. Characterizing the toughness of an epoxy resin after wet aging using compact tension specimens with non-uniform moisture content. *Polymer Degradation and Stability*, 2014, 109: 319-326.

[33] Borges RC. *Durability of GFRP Pultruded Profiles made of Unsaturated Polyester and Vinylester Resins*. Master dissertation in Civil Engineering (in portuguese), Instituto Superior Técnico, 2014.

[34] Balouch SU, Forth JP, Granju JL. Surface corrosion of steel fibre reinforced concrete. *Cement and Concrete Research*, 2010; 40(3): 410–414.

[35] Granju JL, Balouch SU. Corrosion of steel fibre reinforced concrete from the cracks. *Cement and Concrete Research*, 2005; 35(3): 572–577.

[36] Frazão C, Barros J, Camões A, Alves AC, Rocha L. Corrosion effects on pullout behavior of hooked steel fibers in self-compacting concrete. *Cement and Concrete Research*, 2016; 79: 112–122.

[37] Silva MAG, Biscaia HC. Effects of exposure to saline humidity on bond between GFRP and concrete. *Composite Structures* 2010; 93: 216-224.

[38] Biscaia HC, Silva MAG, Chastre C. An experimental study of GFRP-to-concrete interfaces submitted to humidity cycles. *Composite Structures* 2014; 110: 354-368.

[39] Mendes PJD, Barros JAO, Sena-Cruz J, Teheri M. Influence of fatigue and aggressive exposure on GFRP girder to SFRSCC deck all-adhesive connection. *Composite Structures* 2014; 110: 152-162.

[40] ISO 527:1997. *Plastics – Determination of tensile properties.* International Organization for Standardization (ISO), Genève; 1997.

[41] ASTM D 695. *Standard test method for compressive properties of rigid plastics*. American Society for Testing and Materials (ASTM), West Conshohocken, Pennsylvania; 2002.

[42] Hodgkinson JM (Editor), *Mechanical testing of advance fiber composites*, CRC Press, Boca Raton, California, 362 p; 2000.

[43] LNEC Test Specification E 397. *Determination of elasticity modulus in compression*. National Laboratory of Civil Engineering (LNEC), Lisbon; 1993 (*in Portuguese*).

[44] EN 12390-6 *Testing hardened concrete – Part 6: Tensile splitting strength of test specimens*. European Committee for Standardization (CEN), Brussels; 2009.

[45] EN 12390-3 *Testing hardened concrete – Part 3: Compressive strength of test specimens*. European Committee for Standardization (CEN), Brussels; 2001.

[46] S&P Clever Reinforcement Company AG. *S&P Resin 220 epoxy adhesive – two-component epoxy resin-based adhesive for S&P FRP Systems*. Technical data sheet; 2013.

[47] Firmo JP, Correia JR, Pitta D, Tiago C, Arruda M. Bond behavior between near-surface-mounted (NSM) CFRP strips and concrete at high temperatures. *Journal of Composites for Construction* 2014, 19(4), 2015.

[48] Roquette MG. *Influence of elevated temperatures on CFRP strengthening systems*,

MSc Dissertation in Civil Engineering, Instituto Superior Técnico, University of Lisbon, 2017.

[49] CEN. Eurocode 4: Design of composite steel and concrete structures - Part 1-1: General rules and rules for buildings. European Committee for Standardization (CEN), Brussels; 2004.

[50] Baltazar L, Santana J, Lopes B, Rodrigues MP, Correia JR, "Surface skin protection of concrete with silicate-based impregnations: Influence of the substrate roughness and moisture". *Construction and Building Materials* 2014, 70:191-200.

[51] EN 1766 *Products and systems for the protection and repair of concrete structures - Test methods - Reference concretes for testing*. European Committee for Standardization (CEN), Genève, 2000.

[52] EN 13687-3 *Products and Systems for the Protection and Repair of Concrete Structures - Test Methods; Determination of Thermal Compatibility - Part 3: Thermal Cycling without De-Icing Salt Impact*. European Committee for Standardization (CEN), Genève, 2002.

[53] Sousa JM, Correia JR, Fonseca SC, Marinho C, Barros PC, Branco F. Durability of connections between GFRP pultruded profiles with structural adhesives (in portuguese). In *5as Jornadas Portuguesas de Engenharia de Estruturas* (JPEE). Lisbon, 2014.

[54] Sousa JM, Fonseca SC, Correia JR, Branco F. Durability of adhesively bonded structural connections between GFRP pultruded profiles (in portuguese). In XI*II Congresso Latino-Americano de Patologia da Construção* (CONPAT). Lisbon, 2015.

[55] CEN. Eurocode 2: Design of concrete structures - Part 1-1: General rules and rules for buildings. European Committee for Standardization (CEN), Brussels; 2004.

[56] Klamer E. *Influence of temperature on concrete beams strengthened in flexure with CFRP*, PhD thesis in Civil Engineering, Eindhoven University of Technology,

Eindhoven, Netherlands, 2009.

[57] Bank LC. Composites for Construction: Structural design with FRP materials. New Jersey: John Wiley & Sons Inc., 2006.

[58] Morgado T, Silvestre N, Correia JR. Simulation of fire resistance behaviour of pultruded GFRP beams – Part I: Models description and kinematic issues. Composite Structures 2018, 187: 269–280.

[59] Cabral-Fonseca S. *Durability of composite materials of polymeric matrix reinforced with fibres used in the rehabilitation of concrete structures* (in Portuguese), PhD thesis in Science and Engineering of Polymers, Minho University, 2008.

[60] SIMULIA. ABAQUS 6.11 - Analysis User's Manual. Dassault Systèmes, Maastricht.

[61] Jones RM. *Mechanics of composite materials*. 2nd Ed., Taylor and Francis Ltd., London, 1999.

[62] Wang YC. Deflection of steel-concrete composite beams with partial shear interaction. *Journal of Structural Engineering* 1998; 124(10): 1159-1165.

Figures captions

Figure 1 – Geometry of the test specimens.

Figure 2 – Specimen preparation: a) roughening of the SFRSCC surface; b) application of the epoxy adhesive; and c) final aspect of the specimens.

Figure 3 – Thermal cycle ageing: target and achieved (measured in the chamber) temperature curves.

Figure 4 – Thermal cycle ageing: target and achieved (measured in the chamber) RH curves.

Figure 5 – Test setup.

Figure 6 – Load *vs*. relative displacement curves representative of each test series.

Figure 7 – Typical failure modes: a) debonding on the SFRSCC (cohesive failure); b) debonding on the epoxy (adhesive failure); and c) web-flange junction rupture.

Figure 8 – Failure load *vs*. duration of thermal cycles ageing: experimental and numerical results.

Figure 9 – Stiffness *vs*. duration of thermal cycles ageing: experimental and numerical results.

Figure 10 – Failure load *vs*. duration of wet-dry cycles ageing: experimental and numerical results.

Figure 11 – Stiffness *vs*. duration of wet-dry cycles ageing: experimental and numerical results.

Figure 12 – Bi-linear shear bond-slip law adopted.

Figure 13 – Overview of the finite element models.

Figure 14 – Evolution of the calibration parameters τ_{max} and d_{soft} with the number of

Tables captions

Table 1 - Main mechanical properties of the GFRP pultruded profiles.

Table 2 – SFRSCC mix composition (kg/m^3).

Table 3 – Experimental series: ageing process, period, number of cycles, number of specimens, failure load (F_u), stiffness (K) and failure mode.

Table 4 – Summary of the calibration of the bond-slip law parameters, numerical results and relative difference to experimental data (Δ).

Table 5 – Elastic properties of the materials used in the FE models.

Figures

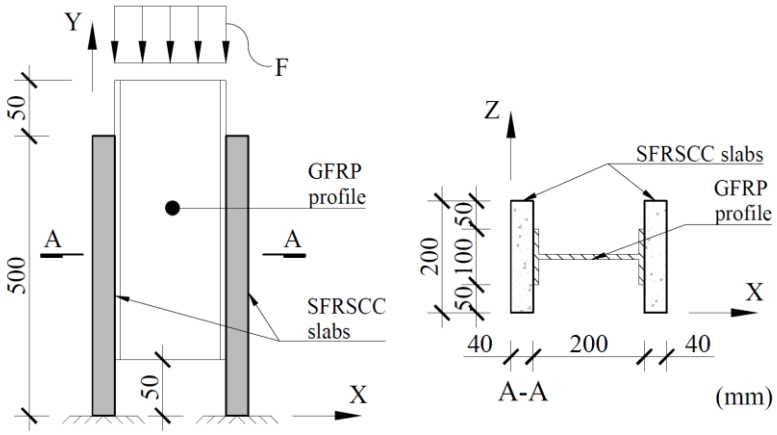

Figure 1 – Geometry of the test specimens.

Figure 2 – Specimen preparation: a) roughening of the SFRSCC surface; b) application of the epoxy adhesive; and c) final aspect of the specimens.

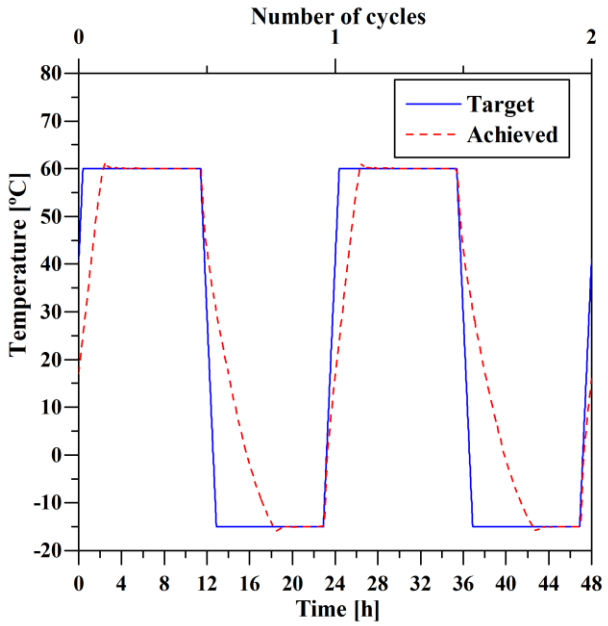

Figure 3 – Thermal cycle ageing: target and achieved (measured in the chamber) temperature curves.

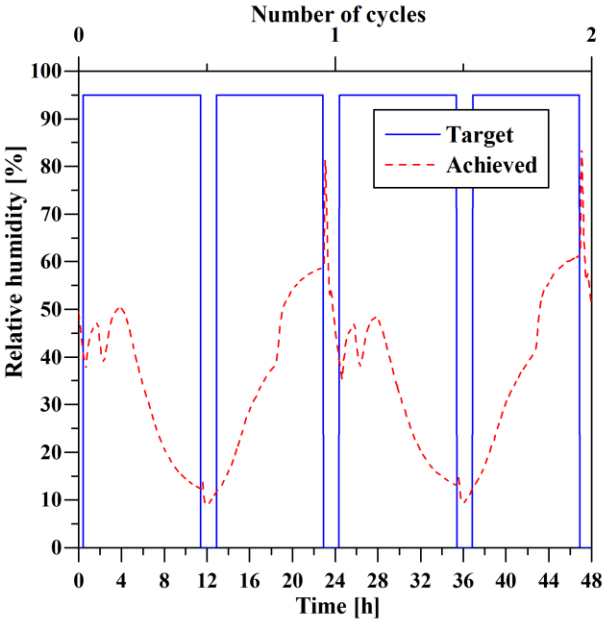

Figure 4 – Thermal cycle ageing: target and achieved (measured in the chamber) RH curves.

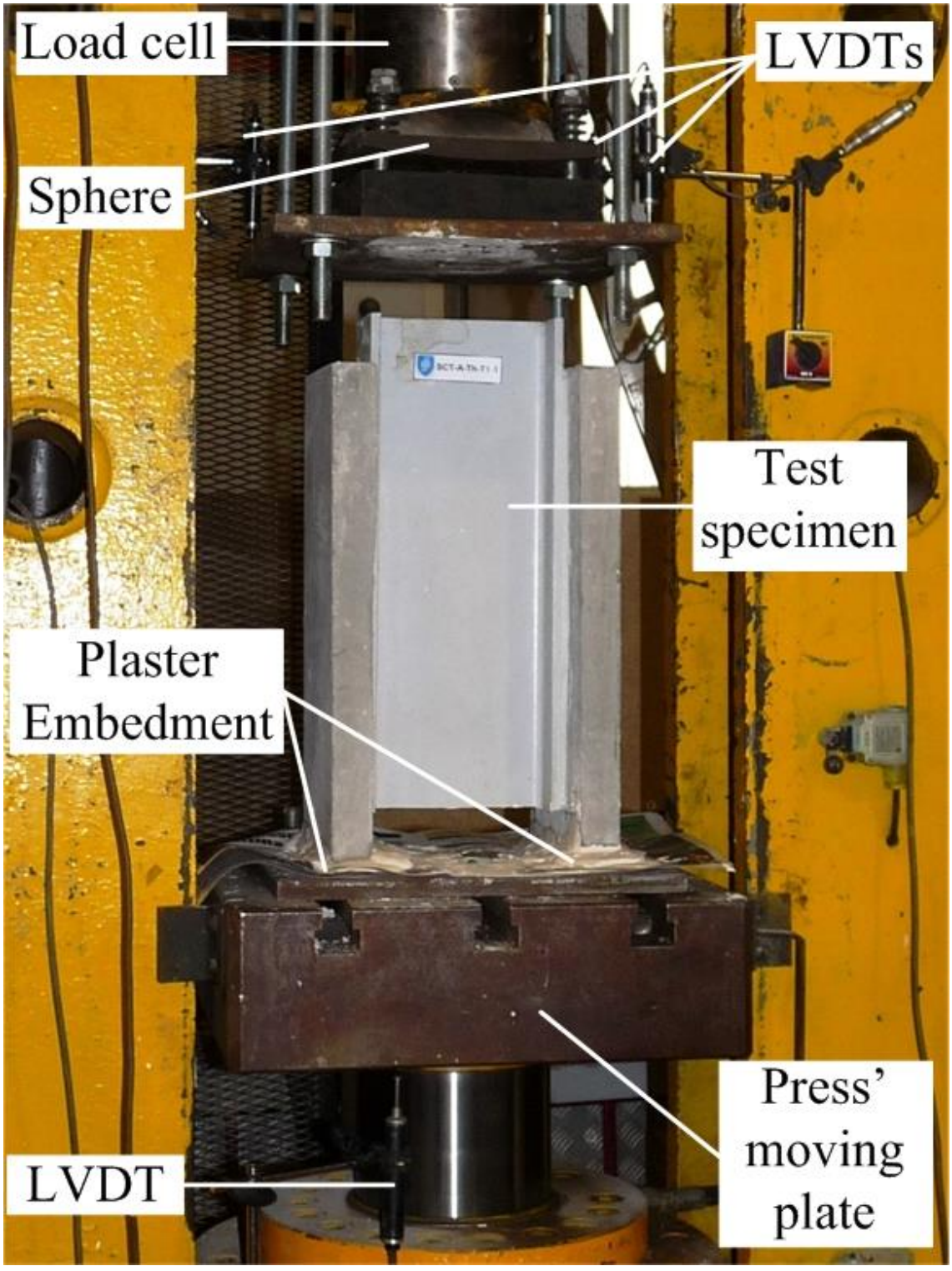

Figure 5 – Test setup.

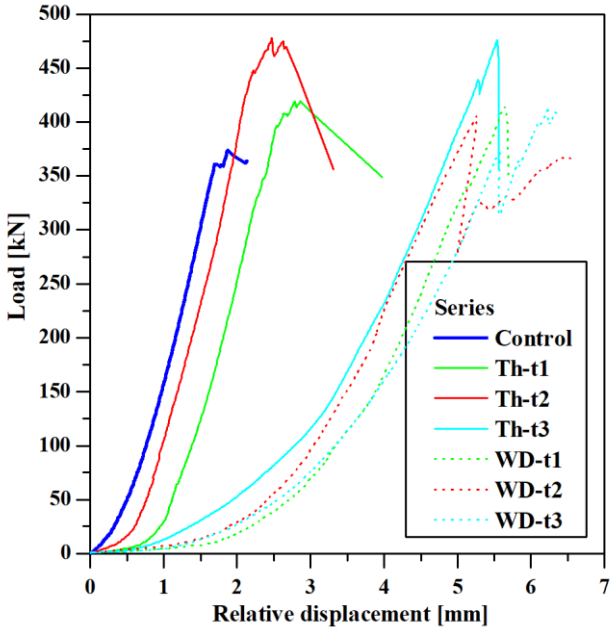

Figure 6 – Load *vs*. relative displacement curves representative of each test series.

Figure 7 – Typical failure modes: a) debonding on the SFRSCC (cohesive failure);

b) debonding on the epoxy (adhesive failure); and c) web-flange junction rupture.

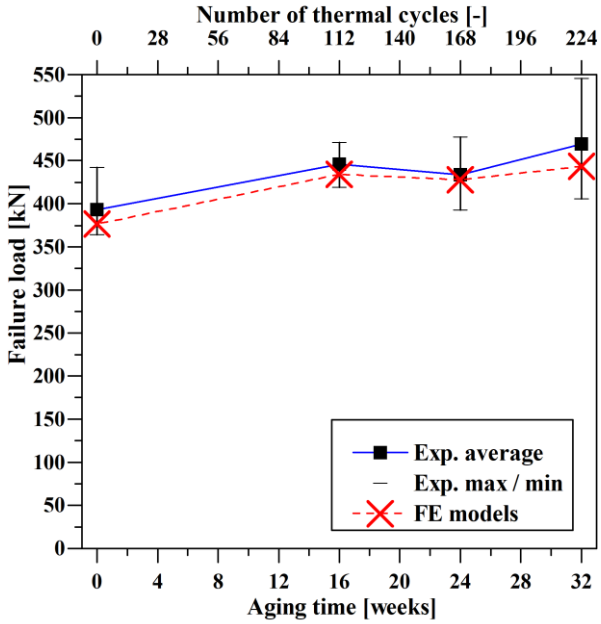

Figure 8 – Failure load *vs*. duration of thermal cycles ageing: experimental and numerical results.

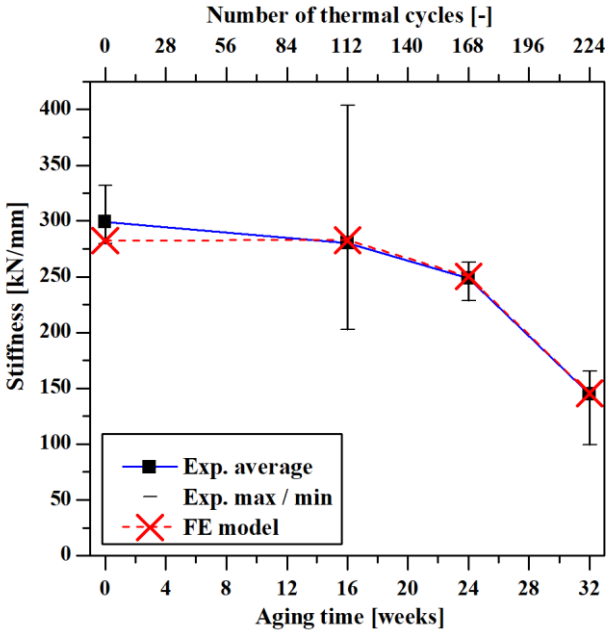

Figure 9 – Stiffness *vs*. duration of thermal cycles ageing: experimental and numerical results.

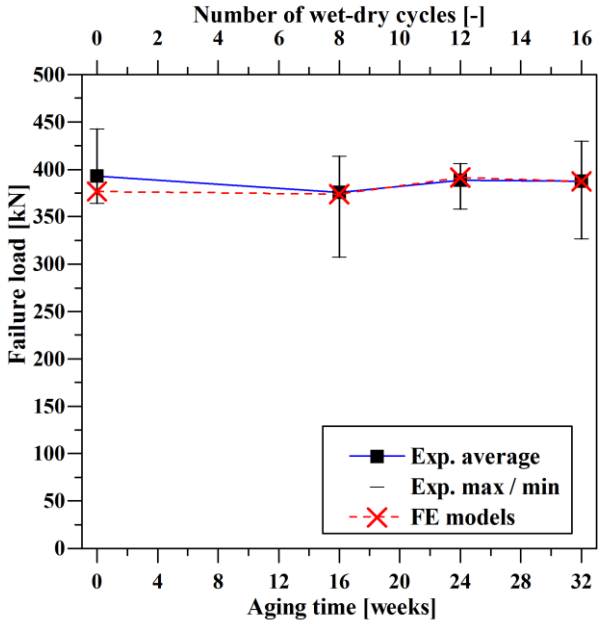

Figure 10 – Failure load *vs*. duration of wet-dry cycles ageing: experimental and numerical results.

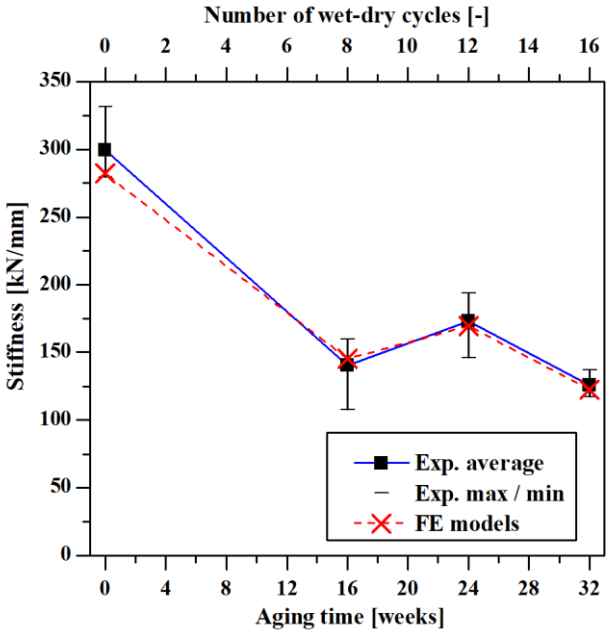

Figure 11 – Stiffness *vs*. duration of wet-dry cycles ageing: experimental and numerical results.

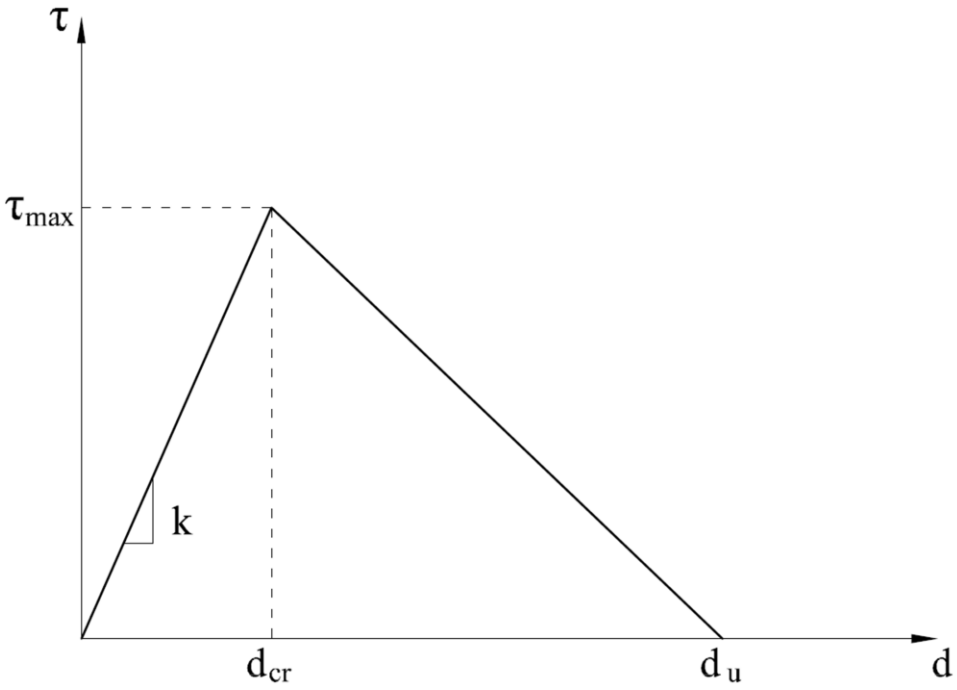

Figure 12 – Bi-linear shear bond-slip law adopted.

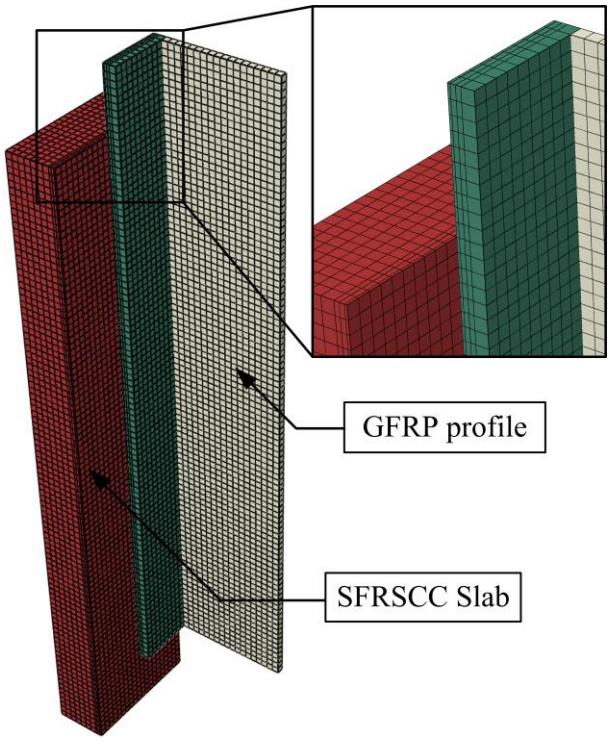

Figure 13 – Overview of the finite element models.

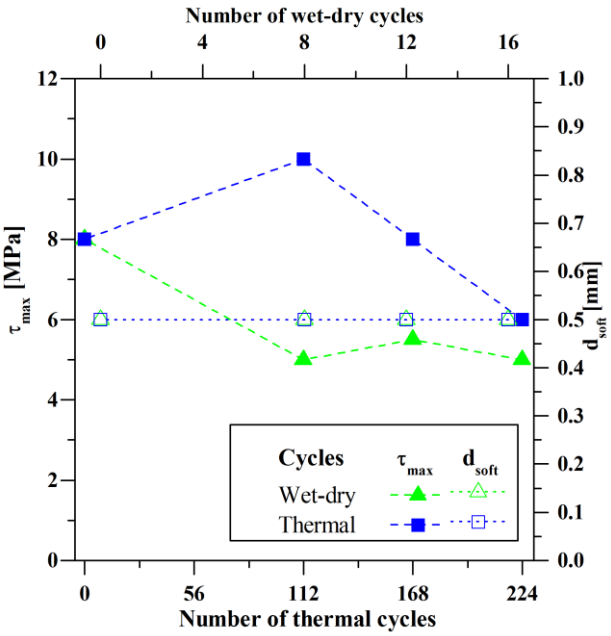

Figure 14 – Evolution of the calibration parameters τ_{max} and d_{soft} with the number of ageing cycles.

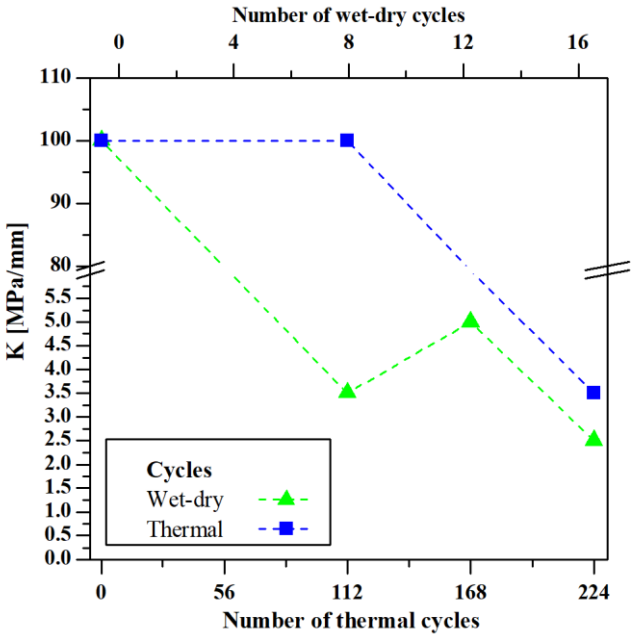

Figure 15 – Evolution of the calibration parameter K with the number of ageing cycles.

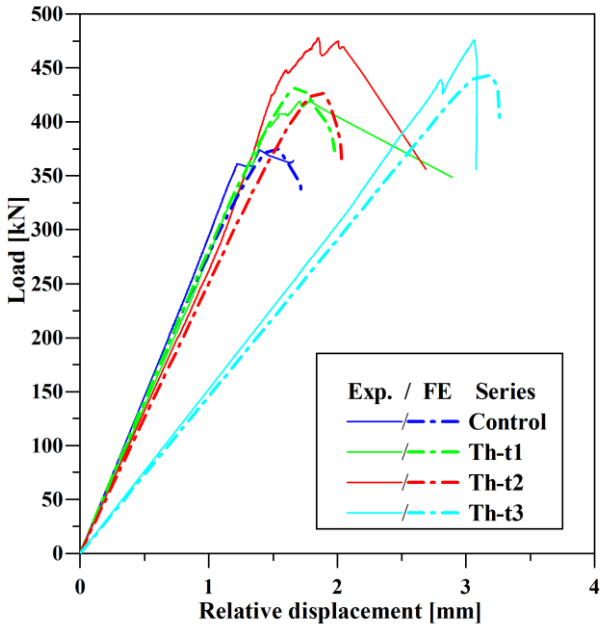

Figure 16– Thermal cycles series load *vs*. relative displacement curves: experimental and numerical results.

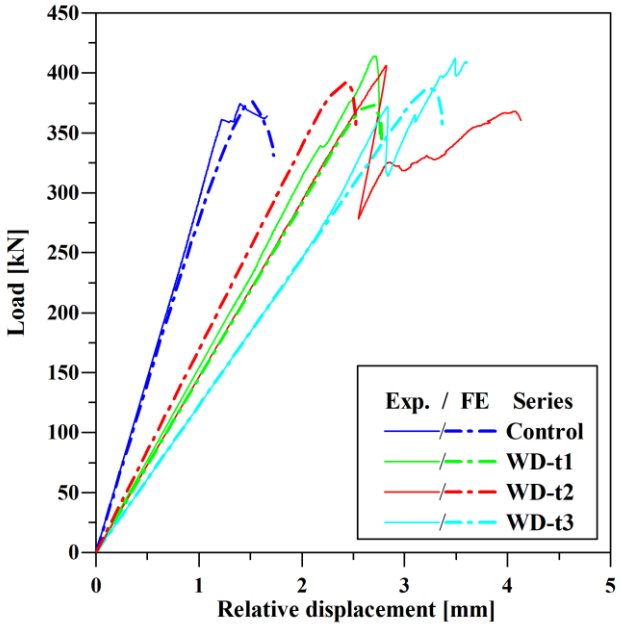

Figure 17 – Wet-dry cycles series load *vs*. relative displacement curves: experimental and numerical results.

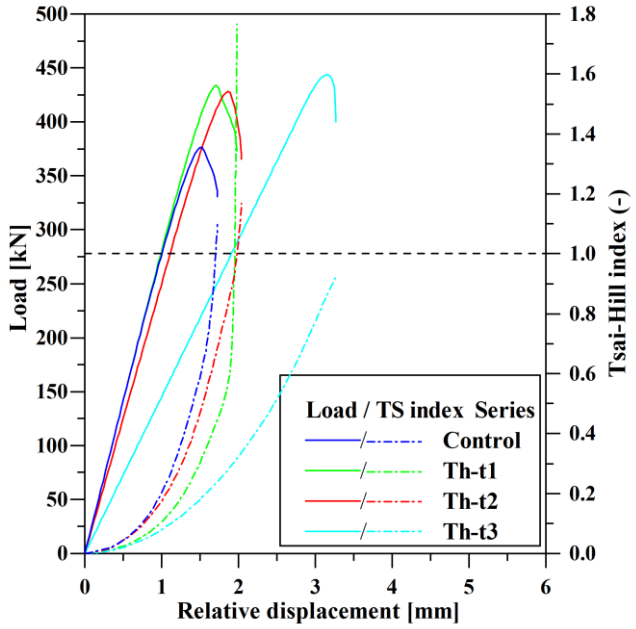

Figure 18 – Thermal cycles series load and Tsai-Hill (TS) index *vs*. relative displacement curves obtained with the FE model.

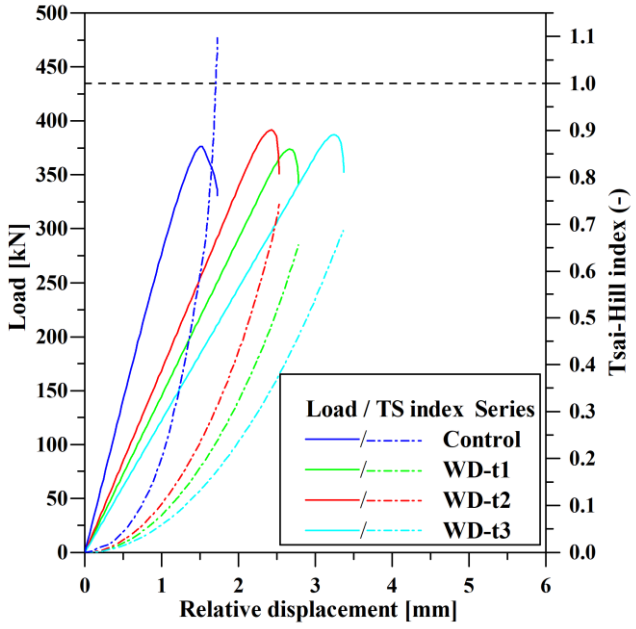

Figure 19 – Wet-dry cycles series load and Tsai-Hill (TS) index *vs*. relative displacement curves obtained with the FE model.

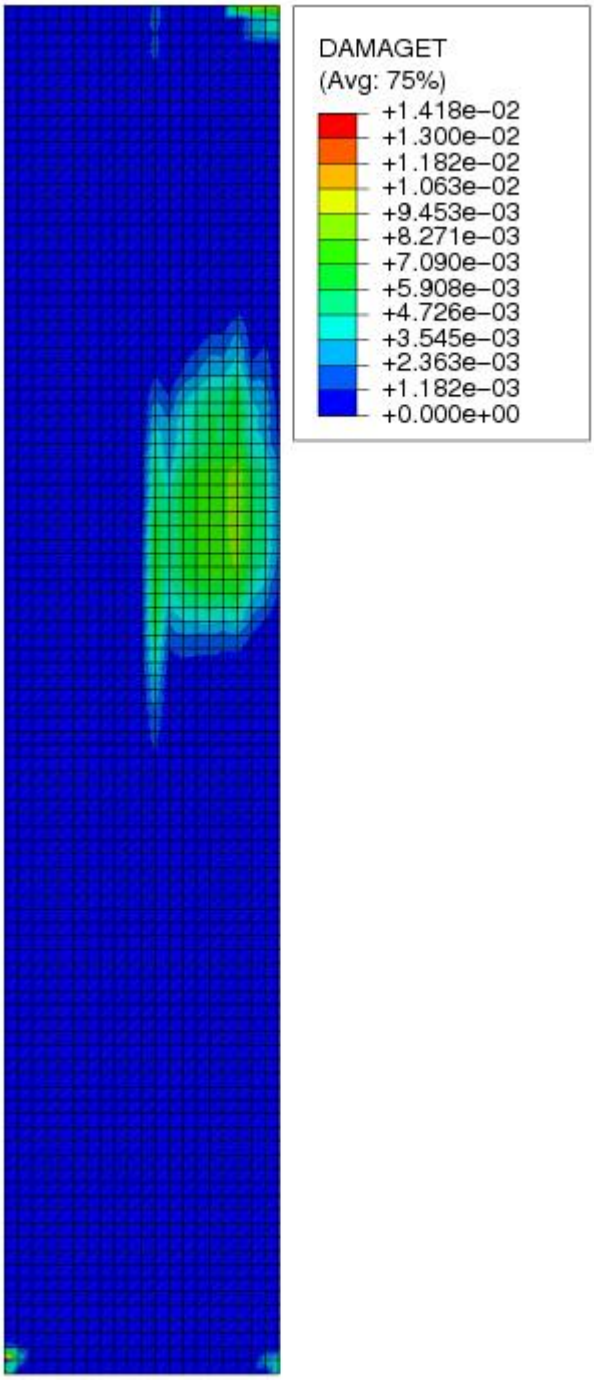

Figure 20 – SFRSCC tensile damage in the FE model for the Control series (unitless).

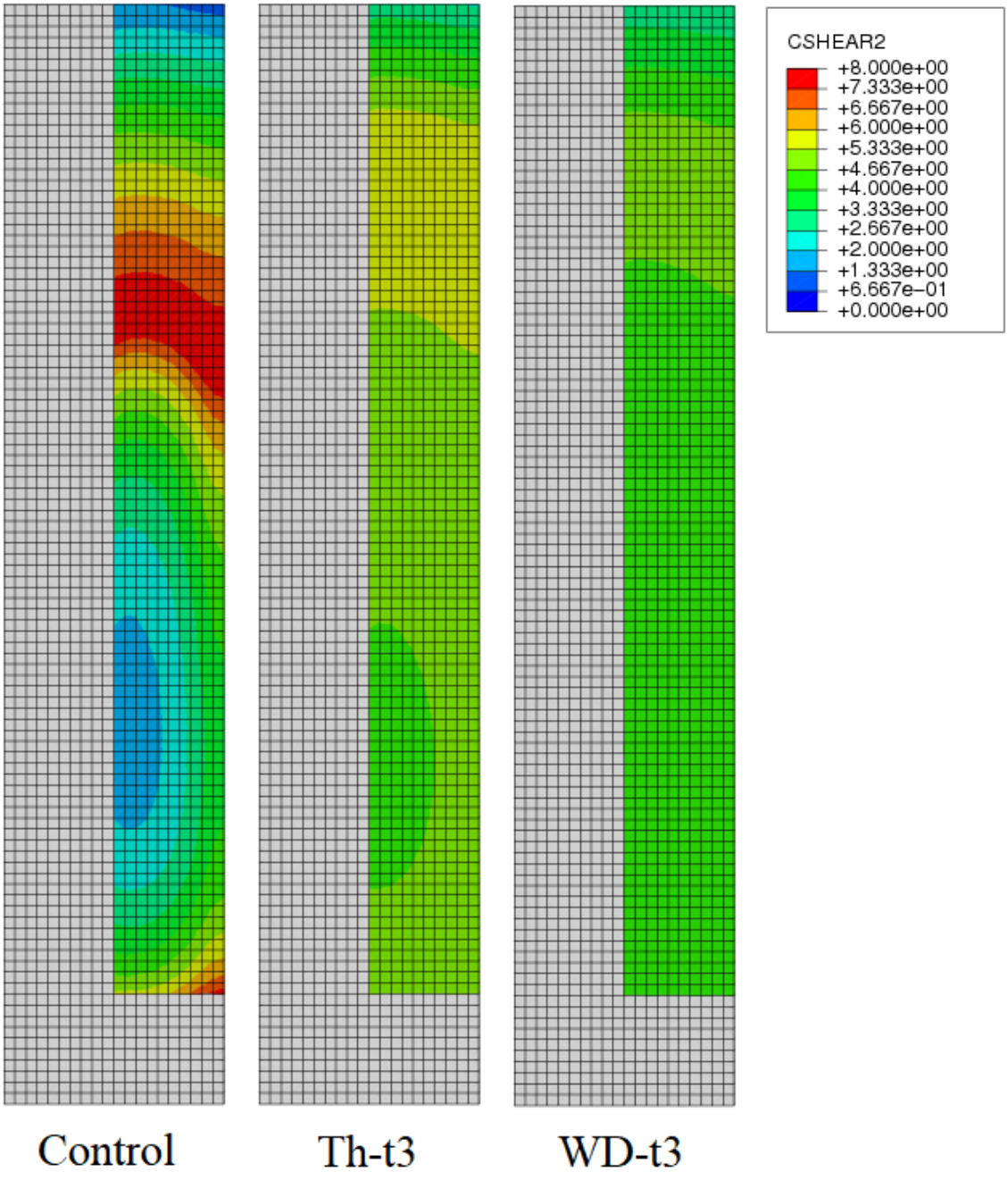

Figure 21 – Shear distribution at the interface: comparison between FE models with calibration parameters for Control, Th-t3 and WD-t3 series (in MPa).

Figure 22 – São Silvestre Bridge (Pontalumis project), Ovar, Portugal.

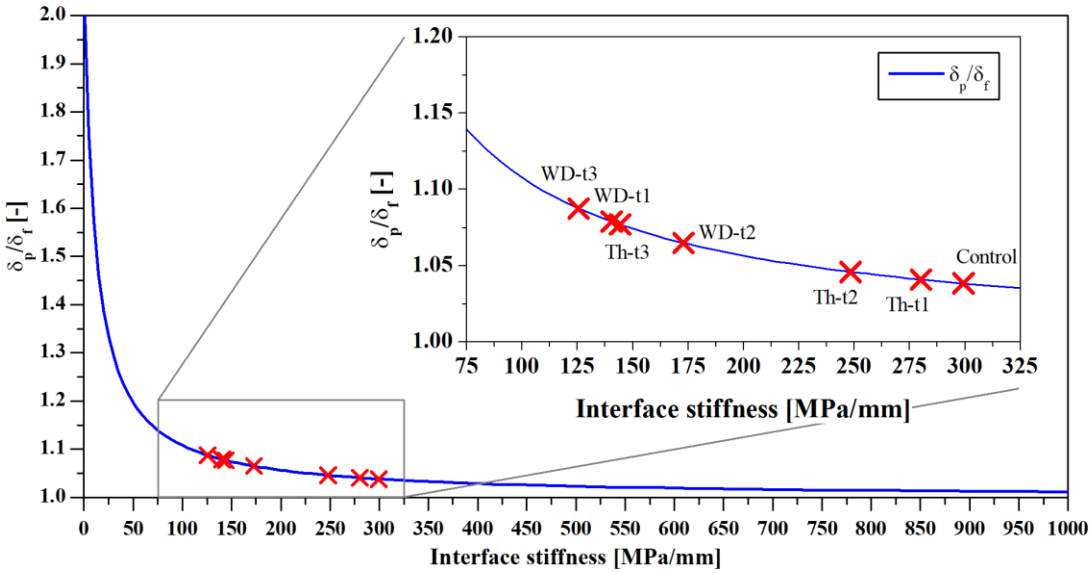

Figure 23 – Evolution of the partial to full shear interaction mid-span deflections with the shear interface stiffness.